

VIP Very Important Paper

www.batteries-supercaps.org

Regulating and Unraveling Electrochemical Behavior of Hierarchically-Densifying Mesoporous Apocynum Carbon for High performance Supercapacitor

Qijun Tong⁺^[a], Zhihao Zhang⁺^[a], Qitian Luo,^[a] Kai Gu,^[a] and Weiqing Yang^{*[a, b]}

The commercial carbon-based supercapacitor with high power ability ($\sim 5 \text{ kW kg}^{-1}$) is still unable to fulfill the superhigh power requirement of specific power-type equipments ($> 20 \text{ kW kg}^{-1}$), such as rail transit facilities, electromagnetic and laser equipment. To unravel the structure-activity relationship and electrochemical behavior of power-type densifying carbon is a key to overcome the contradiction of the suitable mesoporous ratio and highly-densifying features toward the superhigh power requirement. Here, we built the hierarchically-densifying mesoporous apocynum carbon (HDMC) with optimized mesoporous ratio by hierarchical activation method. More importantly, both the isothermal desorption/adsorption and high-pressure mercury intrusion porosimetry methods were employed to synergistically uncover the microscopic surface carbon network stacking mechanism and the macroscopic carbon skeleton

densification assembly mechanism. The highly-densifying skeleton features and high mesoporous ratio properties were proved to be co-existed in HDMC, which is in favour of rapidly ion/electron transferring toward electrochemically-improving power behavior of HDMC. A combination of high tap density (0.387 g cm^{-3}) and ideal microporous-mesoporous system (23.1% proportion of mesoporous) have taken this HDMC to provide a super-high power density (33.5 kW kg^{-1}) and a high volume power density (9.37 kW L^{-1}) for HDMC-based supercapacitor, more than those of commercial YP-50F (14.9 kW kg^{-1} @ 4.63 kW L^{-1}). Therefore, this work provides a synergistic strategy to incorporate the properties of mesoporous and densifying, and reveals its electrochemical behavior toward the further application of power-type supercapacitors.

1. Introduction

Porous carbon with high specific surface area (SSA) and high conductivity is ideal electrode material for supercapacitors. At present, commercial carbon-based supercapacitors could provide power density of $\sim 5 \text{ kW kg}^{-1}$ ^[1,2]. However, the present porous carbon could not provide the optimal interface/pore characteristics for rapidly charge-transferring of carbon-based supercapacitor and difficultly meet the higher performance requirements of specific power-type equipment ($> 20 \text{ kW kg}^{-1}$), such as rail transit facilities, high-power start-stop motors, electromagnetic and laser equipment.^[3,4] It cries for a way of constructing hierarchical carbon structure with ideal mesoporous ratio/high density properties and revealing the kinetic mechanism of its rapid electron migration/ion transport.^[5] For the electrochemical mass transport process of power-type supercapacitor, the ideal carbon-based electrode not only requires sufficient adsorption sites, but also requires high ion adsorption-desorption and electron transfer efficiency.^[6,7] On

the one hand, porous carbon with ideal mesoporous ratio provide sufficient reaction surface area and more efficient ion-transport channels.^[8] On the other hand, faster and more efficient electron transferring ask more sufficient interface contact between electrode particles, which could be described as constructing densifying skeleton.^[9] However, the properties of high mesoporous proportion and high-density are often contradictory. Further, the mesopores carbon network with larger pore volume mostly provide lower density surface stacking mode at micro-level, the loose and discontinuous carbon layer are introduced in skeleton system, which result in low density at macro-level, and electrochemical instability for supercapacitor with higher performance requirements.^[10,11] Therefore, regulating hierarchical densified mesoporous carbon while unraveling its electrochemical behavior for the application of high-power supercapacitor is still a big challenge to be resolved.

The excellent electrochemical behavior of power performance for hierarchical densifying mesoporous carbon (HDMC) could be explained by its co-existing structures of high-density continuous carbon skeleton and hierarchical mesopores. This synergistic and coupling properties show advantages for supercapacitor in efficient ion/electron transport, high electrochemical stability and higher volume performance, as follows: i) The densifying skeleton of HDMC build an electronic network with high conductivity, while the hierarchical pore ensure large and rapid transportation of ions. This synergistic mechanism of hierarchical-densification system enhance the high-power ion/electron store performance of supercapacitor by reducing the interface resistance and improving the mass transfer

[a] Q. Tong,⁺ Z. Zhang,⁺ Q. Luo, K. Gu, W. Yang
Key Laboratory of Advanced Technologies of Materials, Ministry of Education, School of Materials Science and Engineering, Southwest Jiaotong University, Chengdu 610031, China
E-mail: wqyang@swjtu.edu.cn

[b] W. Yang
Research Institute of Frontier Science, Southwest Jiaotong University, Chengdu 610031, China

[+] These authors contributed equally to this work.

Supporting information for this article is available on the WWW under <https://doi.org/10.1002/batt.202400450>

efficiency.^[12–14] ii) Constructing carbon skeleton with higher density and narrowing the interface spacing, the utilization efficiency of carbon particles stacking space are improved at macro-scale, which provide higher power/energy density than the traditional high mesoporous ratio carbon.^[15,16] iii) Continuous and dense carbon skeleton optimizes the electron transferring path and homogenizes the charge distribution, while hierarchical mesopores with low tortuosity further reduces the pore wall pressure in the mass transfer process by reducing the diffusion resistance. Thus, HDMC show long electrochemical cycle life and ideal environment stability at high power performance.^[17,18] iv) Larger proportion of mesopores provide infiltrative channel for the quicker transferring in liquid phase, which reduces the amount of electrolyte for the requirement of maintaining the same capacitance, while densifying skeleton with high intrinsic conductivity could also construct electrode network at a lower conductive agent ratio. This high specific volume performance can fill the requirement of higher energy/power density simultaneously. Although many reported methods such as composite polymer, template-assisted or precursor-derived method could build densifying carbon skeleton,^[19–21] construct hierarchical pore,^[22,23] or altering the average pore size.^[24,25] However, these methods are difficult to obtain the dual properties of high density and high mesoporous ratio synchronously. There are limitations in uncontrollable activation for surface unstable carbon layer and unproven electrochemical synergy working mechanism between densifying skeleton and hierarchical mesoporous system.^[26,27] Therefore, to design high power performance of HDMC supercapacitor not only require synchronously building the optimal ratio of mesopores and micropores with high density and dense carbon skeleton, but also require unravelling the electrochemical mechanism of these properties toward improving charge transfer behavior. We noted that some iron-based activators show preferable catalytic decomposition activity to carbon precursor, which could efficiently etch a controllable proportion of mesopores by regulating the interface reaction of the carbon surface layer. Even so, for higher density performance, the obtained porous carbon still needs to adjust its rough stacking mode at microscopic, and HDMC require more precisely construct carbon skeleton at different scales.^[28–30] Meanwhile, the electrochemical behavior between different micro/mesoporous proportion, skeleton densities and particle packing types should be revealed.

Here, we embedded composite iron-based activators into biomass precursor, hierarchical micro-mesoporous system was built at first-activation, and densifying carbon skeleton were constructed at second-activation. This multi-dimensional precise interface construction strategy can simultaneously regulate compactness and pore hierarchy properties of HDMC. Through directional etching, some weak carbon skeletons are broken and reorganized, integrating and standardizing the geometry and pore distribution of carbon skeletons. In fact, the carbon skeleton is more stable after the second activation. Resulted, HDMC provide both optimal mesoporous proportion (23.1%) and high density (0.387 g cm⁻³). It was also proved that the densifying HDMC provide high SSA of 2130 m² g⁻¹ and high

conductivity of 2.60 × 10³ S m⁻¹. Benefiting from the above excellent physical performance, HDMC-based symmetric supercapacitors demonstrate super-high power density of 33.5 kW kg⁻¹ with considerable energy density of 8.05 Wh kg⁻¹. Moreover, HDMC-based soft packaging supercapacitors provide higher volume power performance of 9.37 kW L⁻¹ or higher volume energy density of 11.0 Wh L⁻¹ than the commercial carbon (YP-50F) based supercapacitor (4.63 kW L⁻¹ @ 7.49 Wh L⁻¹). Obviously, HDMC exhibit ideal hierarchical mesoporous structure and densifying stacking property. More importantly, excellent power-type electrochemical behavior in more efficient charge transfer mechanism was been proved to be attributed to the synergistic matching of hierarchical pores and densifying skeletons, which could be ascribed to be its hierarchically wide-size pore channels. These shortening ion transport paths provide excellent ionic conductivity, and densified carbon skeleton structures with high continuity provide superior electronic conductivity. Therefore, HDMC could present the high-power and high specific volume performances. The low cost and large-scale preparation of HDMC is hopeful prospect for applying in power-type high-density energy storage equipment.

2. Results and Discussion

Apocynum venetum, a species of the Apocynaceae family, is known for its high cellulose content and possesses an excellent primitive interconnected sieve tube structure. The fiber skeleton surface exhibits horizontally interconnected porous channels, which can provide conditions for the full impregnation of activators and rapid transfer during the high-temperature process. In Figure 1a, the SEM image of original precursor show axial vessels inserted between fiber bundles. After removing colloid substance (Figure 1b, SEM image), the surface of fiber skeleton shows transverse interconnected pore channels. Therefore, the activator could be uniformly embedded into the biomass fiber channel by impregnation strategy, which enhance the diffusion efficiency of the gasified decomposition substances produced by activation and ensure a stable etching reaction. Figure 1c shows the surface morphology and pore structure changes of Fe(N)(K) for first-activation, its irregular carbon skeleton indicate that the original fibers bundles have been fully etched. Meanwhile, there are a large number of macropores (Figure S1a, SEM image) with a diameter of 0.5 to 2 μm exposed on the surface of skeleton. TEM image (Figure 1d) further reveals that these macropores are irregular and interpenetrate each other with different shapes, they constitute the extremely rough surface morphology of Fe(N)(K). Figure 1e shows the SEM morphology of HDMC for second-activation. Compared with the first activated Fe(N)(K), HDMC reveal a more regular geometry of carbon particles, the site of its micron-sized pores is less overlapped, which results in a relatively uniform surface for its particles (TEM image, Figure 1f). Benefiting from the significantly reducing entropy at the surface skeleton structure from second-activation, HDMC could obtain a macroscopic density higher than Fe(N)(N), we define this process as

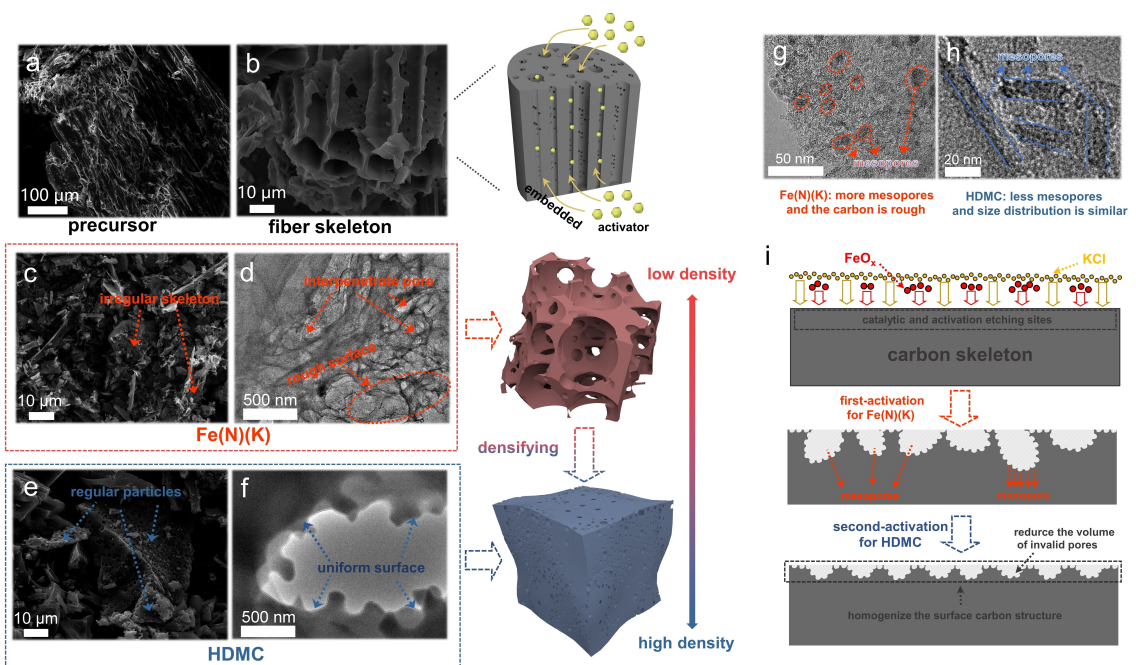
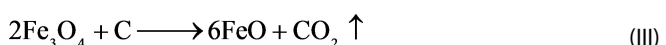


Figure 1. Morphology characterization of porous carbon. **a, b)** Scanning electron microscopy (SEM) images of apocynum fiber. **c) and e)** SEM image of Fe(N)(K) and HDMC. **e) and f)** TEM images and of Fe(N)(K) and HDMC. **g) and h)** H-TEM images for pores structure. **i)** morphology evolution process illustration at micro-scale.

densifying. For pore morphology at nanoscale, both Fe(N)(K) and HDMC show a hierarchically densifying mesoporous/micro-pore system (H-TEM images, Figures 1g and h), which proves that a large number of mesopores are mainly formed at first-activation. Moreover, the mesoporous proportion of HDMC is less than that of Fe(N)(K), revealing the distribution state of its mesopores could be changed by densifying technology.

Hierarchical pores and high-density skeleton properties of HDMC were sequentially constructed by first-activation and second-activation. The construction mechanism of first-activation could be interpreted by the step-by-step redox reaction between FeO_x and C for activation, as follows:



(I) when the temperature exceeds to 125 °C, the embedded $\text{Fe}(\text{NO}_3)_3$ decompose into nanosized Fe_2O_3 particles and continue to uniformly deposit on the surface of the precursor fiber wall; (II) Fe_2O_3 particles mildly etch the fiber skeleton (500–600 °C), some thin and weak positions of the skeleton were collapsed, while the unreacted Fe_3O_4 and reduced Fe_2O_3 particles in collapse site were aggregated. This aggregation behavior plays a positive role in promoting the process of cellulose etching reaction, which caused to the formation of

macropore structure; (III) Fe_3O_4 severely etch the carbonized cellulose (600–700 °C), which mainly occurs on the wall of skeleton and form carbon particles with rough surface morphology. The above inference could be proved by the SEM images of the first-activation at different temperatures of 600~700 °C (Figure S2). It is shown that the irregular micron-sized macropores are mainly formed during the temperature of 600–700 °C. Finally, when the temperature exceeds to 770 °C (melting point of KCl), ionized K^+ fully infiltrate carbon skeleton. Existing FeO_x plays a catalytic role in accelerating the intrusive of K^+ , which relate to the reaction of some free oxygen groups on the carbon surface. This composite catalytic and activation mechanism accelerates the swelling and etching speed of the carbon skeleton by the molten KCl, a large number of micropores are formed. Meanwhile some K^+ are gathered around FeO particles, which sites form mesopores.^[31,32]

Figure 1i shows the densifying mechanism of second-activation for HDMC at micro-scale. Their optimizations of surface morphology and skeleton structure are attributed to the uniform activation for first-activation carbon by the etching and pore-forming effect of low proportion KOH. Part of the weak carbon skeleton was broken and recombined by the directional etching, both geometric shape of carbon skeleton and distribution of pores were integrated and regularized. For micro level, the number of irregular macropores with a lower specific surface area is reduced, but the filling rate of interstitial space in carbon skeleton is increased. While for macro level, the porous carbon becomes a closer-contact carbon particles system, which effectively solved technical challenge of high SSA porous carbon with the low density. This second-activation change the geometry and surface structure of porous carbon

and construct a tight and networked skeleton connection, which system keeps the unified and coexistence of porosity and high-density performance. the thermal stability of the carbon material at high temperature becomes better (Figure S12). Therefore, precisely controlling the local etching and surface restacking process of carbon atoms could promote ideal coexistence properties of hierarchical mesoporous structure and high-density.

To reveal the chemical and physical evolution behavior of HDMC and Fe(N)(K), two additional samples (AC-KOH, YP-50F) were characterized comparatively. Figures S3–S6 and Table S1 presents the element composition by (SEM-EDS) mapping, and the corresponding element distribution and content. Compared with Fe(N)(K), Fe element in HDMC is distributed less and evenly(Table S9). The precise O1s and C1s X-ray photoelectron spectroscopy (XPS) results of overall elemental composition are shown in Figure 2a. As for Table S2, HDMC presented the highest C element ratio (94.74%) and C, O element ratio (C/O= 23.69). Furthermore, in the O1s spectra of HDMC (Figure 2b), the fitting peaks at 283.32 eV, 284.75 eV, 285.88 eV are corresponding to C=C/C=C, C—O, C=O chemical bonds, respectively (Table S3). The C=C/C=C bonds of HDMC are more than those of Fe(N)(K), AC-KOH and YP-50F, evidently proving the higher continuity of carbon skeleton and the full aromatization of cellulose. Meanwhile, the C—O and C=O defects which relate to O element are less shown in HDMC. The element content and chemical bond composition values present a more stable carbon skeleton with higher structural continuity for HDMC. It is proved that the multiple activation strategy should be helpful for improving the purity of porous carbon, and high-strength, continuous, and high-purity skeleton should be beneficial for improving the intrinsic conductivity and relaxing the self-

discharge of its supercapacitor electrode. In addition, the composition of surface functional group was analyzed by fourier transform infrared spectroscopy (FTIR) (Figure 2c). The absorption peaks of 672 cm^{-1} , 1057 cm^{-1} , 1620 cm^{-1} , 2851 cm^{-1} , 2920 cm^{-1} and 3445 cm^{-1} are corresponding to CH bending vibration, C—O stretching vibration, C=C skeleton vibration, —CH₂— stretching vibration, -CH₃ stretching vibration and -OH stretching vibration, respectively. For XPS analysis, the C=C vibration intensity with relation to the skeleton integrity of HDMC is higher than that of Fe(N)(K), and the C—O stretching vibration intensity with relation to the defective structure with incomplete carbonization is lower than that in Fe(N)(K). The above results suggest oxygen group defects should increase during the first-activation and then reduce during the second-activation. On the other hand, -OH bonds of AC-KOH and HDMC are more than that of YP-50F and Fe(N)(K). These -OH bonds are introduced during KOH activation and generally distributed on the surface of carbon.

For the physical and crystalline phase structure of porous carbon, X-ray diffraction (XRD) curves (Figure 2d) shows the wide diffraction peaks at 22° and 43° , corresponding to the (002) and (100) crystal planes of small amount graphite phase, respectively. The wider diffraction peaks of Fe(N)(K) and AC-KOH than HDMC and YP-50F indicate a more disordered pore structure, which is attributed to the more intense etching reaction of carbon during the activation process of Fe(N)(K) and AC-KOH. The XRD curves in 5° – 8° is related to the diffraction between pore walls for some micropores with pore size of 0.553 – 0.883 nm, more micropores correspond to stronger low-angle diffraction. For low angle of 5° – 8° , the lowest diffraction intensity of Fe(N)(K) indicates the first-activation could construct the larger proportion of mesopores. While the medium

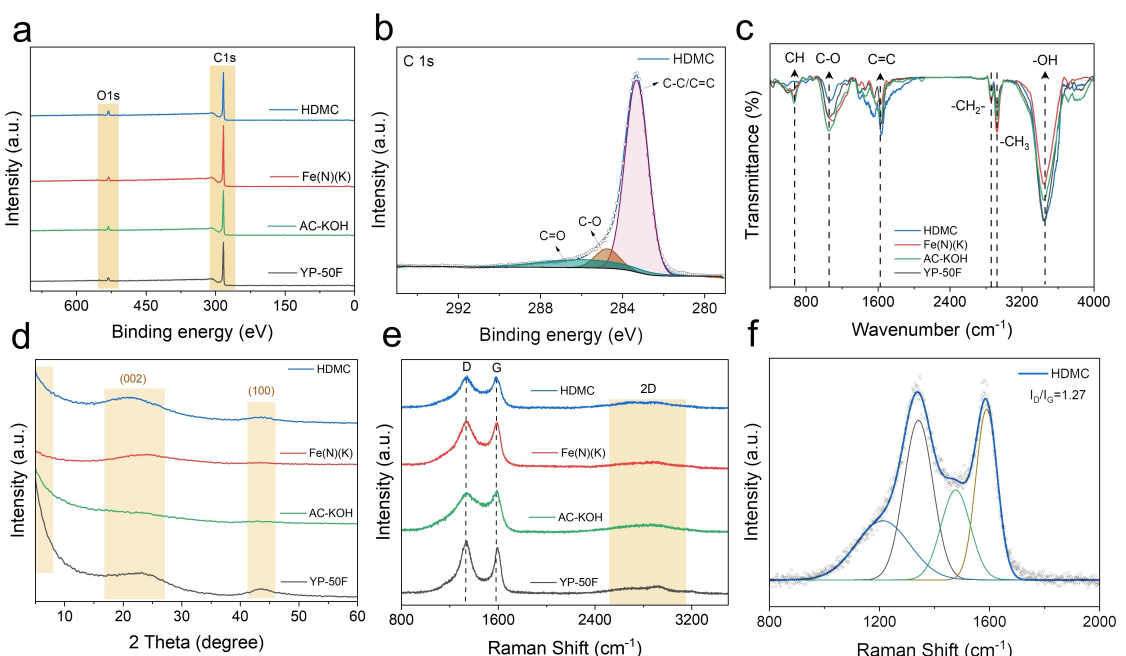


Figure 2. a) Comparison of XPS curves and b) C1s fine spectra analysis for HDMC. c) Comparison of FTIR curves (400 – 4000 cm^{-1}). d) Comparison of XRD curves (5 – 60°). e) Comparison of Raman curves (800 – 3600 cm^{-1}) and f) fitted Raman curve of HDMC.

diffraction intensity of HDMC in $5^\circ\text{--}8^\circ$ evidently reveals the second-activation could construct a right proportion of micro-mesoporous. Raman spectrum characterization reveals the structural defects of porous carbon (Figure 2e). The D peak at 1300° reflects lattice defects of skeleton, and the G peak at 1800° is related to sp^2 -type stretching vibration of C atoms. The I_D/I_G ratio (which reflect the disorder degree for carbon skeleton) of HDMC, Fe(N)(K), AC-KOH and YP-50F are 1.27, 1.40, 1.84 and 1.76, respectively (Figure 2f and Figure S8). The higher I_D/I_G ratio of Fe(N)(K) than HDMC could attributed to the increasing defects of carbon skeleton which caused by the severe FeOx etching reaction during $600\text{--}700^\circ\text{C}$ for first-activation. Among them, the lowest I_D/I_G ratio of HDMC proves that defect could be optimized by the milder reaction of second-activation. All the HDMC, Fe(N)(K), AC-KOH and YP-50F show the wider 2D peak, which prove the stacking type for carbon skeleton is disordered and multi-layer stacking.

Isothermal adsorption/desorption characterization were employed to uncover pore structure and pore distribution. The isothermal curves were shown in Figure 3a. When the relative pressure P/P_0 of 0–0.1, the rapidly increasing adsorption capacity of four samples presents a large number of ultra-micropores and micropores, which contribute the most specific surface area. When P/P_0 of 0.1–0.4 (II), HDMC and Fe(N)(K) demonstrate the higher increments than AC-KOH and YP-50F, indicating the larger proportion of mesopores ($2\text{--}4\text{ nm}$) of the former two. When P/P_0 of 0.4–0.9 (III), isothermal curves of AC-KOH and YP-50F show an adsorption plateau, but HDMC and Fe(N)(K) curves show obvious increase, which can be mainly derived from the adsorption behavior of mesopores with the size of $4\text{--}20\text{ nm}$. When P/P_0 of 0.9–0.995 (IV), the increasing curve of Fe(N)(K) is more than that of HDMC, showing excessive proportion of macropores for Fe(N)(K). These macropores

provide the fewer adsorption sites, which is not useful for the density properties of porous carbon. For this reason, the second-activation would partly transform invalid macropores into the hierarchical pores structure for the enhancement of improving the porous carbon density. For desorption branch, both HDMC and Fe(N)(K) show hysteresis loops in III, suggesting the large number of capillary condensed mesopores. In general, the isotherm of HDMC and Fe(N)(K) are close to type-IV typical adsorption characteristics, there is a certain proportion of micropores and mesopores. However, AC-KOH and YP-50F present type-I typical adsorption characteristics, showing the fewer mesopores.

Further, the density functional theory (DFT) method was used to uncover the pore distribution in Figure 3b. All the HDMC, Fe(N)(K), AC-KOH and YP-50F show abundant micropores distributions ($0.6\text{--}2\text{ nm}$), their average pore sizes are 2.551 nm, 3.130 nm, 1.955 nm and 2.005 nm and the corresponding SSA (S_{BET}) are $2130\text{ m}^2\text{ g}^{-1}$, $1980\text{ m}^2\text{ g}^{-1}$, $2273\text{ m}^2\text{ g}^{-1}$ and $1685\text{ m}^2\text{ g}^{-1}$, respectively. As for mesopore ($>2\text{ nm}$), HDMC and Fe(N)(K) demonstrate the larger size and the wider distribution of mesopores, strongly proving the multi-dimensional composite activator can construct mesopores (Table S4).

Figure 3c reveals the relationship between cumulative SSA and pores sizes. For the micropore proportion ($\alpha = S_{\text{micro2}}/S_{\text{total}}$), all the HDMC, Fe(N)(K), AC-KOH and YP-50F present $\alpha_{\text{HDMC}} = 69.5\%$, $\alpha_{\text{Fe(N)(K)}} = 62.8\%$, $\alpha_{\text{AC-KOH}} = 75.9\%$ and $\alpha_{\text{YP-50F}} = 96.3\%$, respectively. Meanwhile, Figure 3d reveals the relationship between cumulative volume and pores sizes. For the mesopore proportion ($\beta = V_{\text{meso}}/V_{\text{total}}$), the HDMC, Fe(N)(K), AC-KOH and YP-50F present $\beta_{\text{HDMC}} = 23.1\%$, $\beta_{\text{Fe(N)(K)}} = 23.4\%$, $\beta_{\text{AC-KOH}} = 10.5\%$ and $\beta_{\text{YP-50F}} = 13.3\%$, respectively. HDMC and Fe(N)(K) reveal the lower S_{micro2} and higher V_{meso} than AC-KOH and YP-50F, evidently proving the multi-dimensional activation strategy can

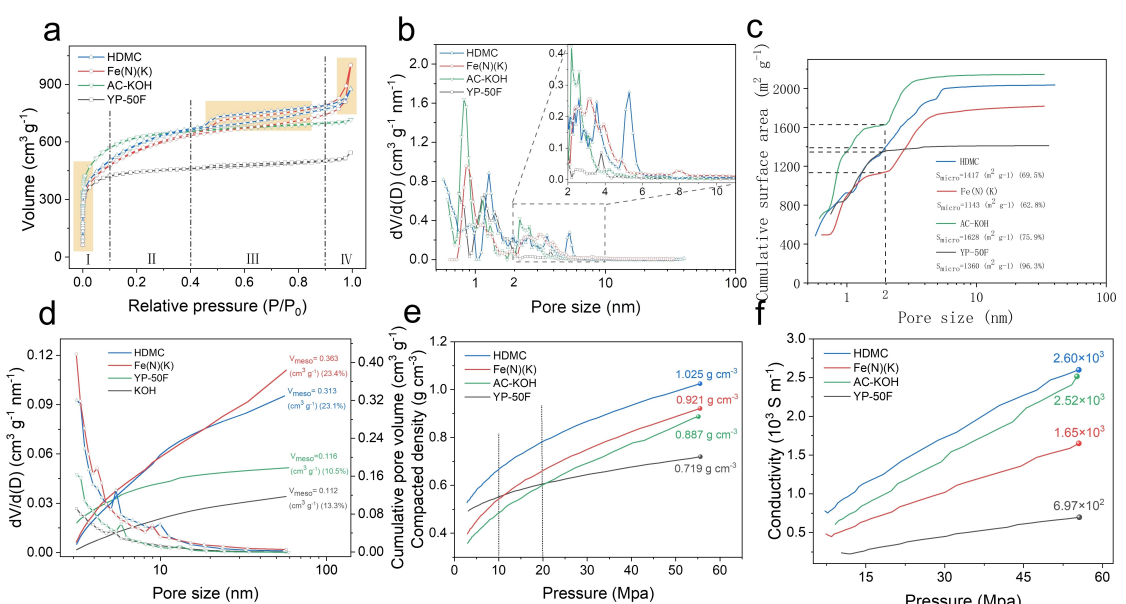


Figure 3. a) Isothermal adsorption/desorption curves of HDMC, Fe(N)(K), AC-KOH and YP-50 F. b) Pore size distribution analyzed from isothermal curves by DFT method (slit pore, NLDFT equilibrium model). c) The relation between cumulative surface area and pore size analyzed from isothermal curves. d) The relation between cumulative volume and pore size analyzed from isothermal curves by BJH method (adsorption branch). e) Characterization of compacted density at different pressure and f) Characterization of conductivity at different pressure for HDMC, Fe(N)(K), AC-KOH and YP-50F.

build the larger proportion of mesopores. In general, the number of adsorption active sites depends on the SSA, while the adsorption efficiency is mainly affected by pore size.^[33] Since charges are easier to efficiently and rapidly transmit at abundant mesoporous with lower migration energy, the optimal $\alpha_{\text{HDMC}} = 69.5\%$ and $\beta_{\text{HDMC}} = 23.1\%$ are useful for simultaneously enhancing adsorption capacity and adsorption efficiency, this optimized pore structure can demonstrate the more ideal ion transporting behavior of charge-ion pairs at higher current density. The higher mesoporous ratio can present the higher rate performance and electrochemical stability, which enables HDMC present a more ideal electric double layer working mechanism and maintain the higher theoretical specific capacitance simultaneously.

Advantages of densifying carbon electrode for higher volume performance could be strongly proved by the density characteristics. As shown in Figure 3e, HDMC demonstrate the highest compaction density of 1.025 g cm^{-3} at 54 MPa, which reveals the most excellent compactness of its skeleton structure. As the pressure increases, apocynum-based carbon (HDMC, Fe(N)(K), AC-KOH) presented the more rapidly increasing compacted density than that of YP-50F, indicative of the more excellent compressibility and the higher compaction density performance of apocynum-based carbon. Furthermore, the loose density and tap density were shown in Table S5. Among four samples, Fe(N)(K) demonstrates the lowest loose density (0.0437 g cm^{-3}), which could be attributed to its irregular particle shape and rough surface structure caused by the excessively violent etching reaction during first-activation. However, HDMC present the higher loose density of 0.163 g cm^{-3} , suggesting that the low-density and fluffiness-stacking properties of Fe(N)(K) could be improved by second-activation. It is incriminated that the fragility skeleton could be broken and recombined from the weak fiber wall site and form a more regular framework during the uniform second-activation process. On the other hand, HDMC demonstrates the higher tap density of 0.387 g cm^{-3} than Fe(N)(K) (0.127 g cm^{-3}), AC-KOH (0.267 g cm^{-3}) and YP-50F (0.294 g cm^{-3}), revealing the uniform second-activation should reduce the irregularity of carbon skeleton. Resulted, HDMC develop a complete and regular skeleton structure by the multiple pore etching and surface construction process during activation reactions at different scales. The number of irregular macropores decrease and distribute uniformly, which increase skeleton density of HDMC and reduce the interstitial volume of its carbon particles. So, the higher continuity of skeleton-pore structure could be constructed. Figure 3f presents the relationship between conductivity and pressures. HDMC provides the highest conductivity of $2.60 \times 10^3 \text{ Sm}^{-1}$ at 54 MPa, which is ascribed to the higher continuity and high compactness skeleton structure. Such high conductivity is beneficial to the stability of HDMC-based supercapacitor at super-high power load.

To reveal the pore formation mechanism for first-activation, the first activated samples by different temperature (500°C , 600°C , 700°C) were further characterized. As shown in Figure 4a, the isothermal curves of Fe(N)(K)_500 and Fe(N)(K)_600 were almost unchanged, indicating the decomposition reaction

of FeNO_3 and the activation reaction between Fe_2O_3 and C were not fully carried out before 600°C . Fe(N)(K)_700 show the larger adsorption capacity in IV and obvious hysteresis loop in III, which is incriminated by the Fe_2O_3 molecules get working to etch carbon skeleton. So, the abundant micron-sized pores and part of mesopores were formed when the temperature reaches to 700°C . Fe(N)(K) shows rapid increase for adsorption capacity in I, II and III region, proving more micropores and mesopores. These micropores are not only related to the multistage reaction of FeO_x molecules, but also incriminated to KCl molecules which play a leading role on the surface etching reaction of carbon skeleton. Also, the above pore-etching theory could be proved by pore distribution results (Figure 4b). There are few micropores and mesopores shown in Fe(N)(K)_500 and Fe(N)(K)_600, while a small amount of micropores and mesopores were shown in Fe(N)(K)_700, and the lager number of micropores and mesopores were shown in Fe(N)(K).

High-pressure mercury intrusion porosimetry (MIP) method can provide the larger measuring range to characterize pore distribution, as shown in Figure 4c (MIP curves), Figure 4d (pore distribution) and Table S6 (pore parameters). For pressure sector of I ($0\text{--}50$ psia), Fe(N)(K), Fe(N)(K)_700 and Fe(N)(K)_500 demonstrate the higher cumulative intrusion volume than HDMC. It could be explained as the excessive activation and etching reaction caused by $\text{Fe}(\text{NO}_3)_3$ and KCl activator during first-activation. As the temperature increases, the pore and skeleton gradually collapse and break. So, the interstitial pore volume increases with the appearance of incomplete skeleton structure and irregular surface. For pore size between $5\text{--}200 \mu\text{m}$, Fe(N)(K) demonstrate the largest pore volume, which relate to its exhibit rough surface and irregular shape induce to larger carbon particles interval volume. While HDMC demonstrate the lowest pore volume, which proves the denser accumulation behavior of carbon particles. For pressure sector of II ($50\text{--}1000$ psia), the median pore diameter (volume) is calculated to be ordered as $\text{Fe}(\text{N})(\text{K})_500 > \text{HDMC} > \text{Fe}(\text{N})(\text{K})_700 > \text{Fe}(\text{N})(\text{K})$, which proved that the first-activation should hierarchically construct different pores size during different temperature stages, while the second-activation could expand carbon wall and increase pore size. Furthermore, for pressure sector of III ($1000\text{--}80000$ psia), the differential pore distribution of mesopores was analyzed by MIP method (Figure 4e). Compared to Fe(N)(K)_500 and Fe(N)(K)_700, HDMC and Fe(N)(K) show more mesopores with the smaller size ($< 10 \text{ nm}$). Average pore diameters (area) of HDMC, Fe(N)(K), Fe(N)(K)_500 and Fe(N)(K)_700 were 3.67 nm , 4.40 nm , 46.71 nm and 52.27 nm , respectively. The higher pore sizes of Fe(N)(K)_700 and Fe(N)(K)_500 is referenced to their few mesoporous structures. Again, these results proved that abundant mesopores were built through the multi-dimensional activation strategy

Density properties of carbon skeleton were also calculated by MIP method (Table S6), HDMC (0.7395 g cm^{-3}) and Fe(N)(K) (0.6999 g cm^{-3}) demonstrate lower apparent densities than Fe(N)(K)_500 (1.1871 g cm^{-3}) and Fe(N)(K)_700 (1.2040 g cm^{-3}), which proved that abundant mesopores of HDMC and Fe(N)(K) were mainly formed at higher temperature ($> 700^\circ\text{C}$) pore-etching process during firstly-activation, and these mesoporous

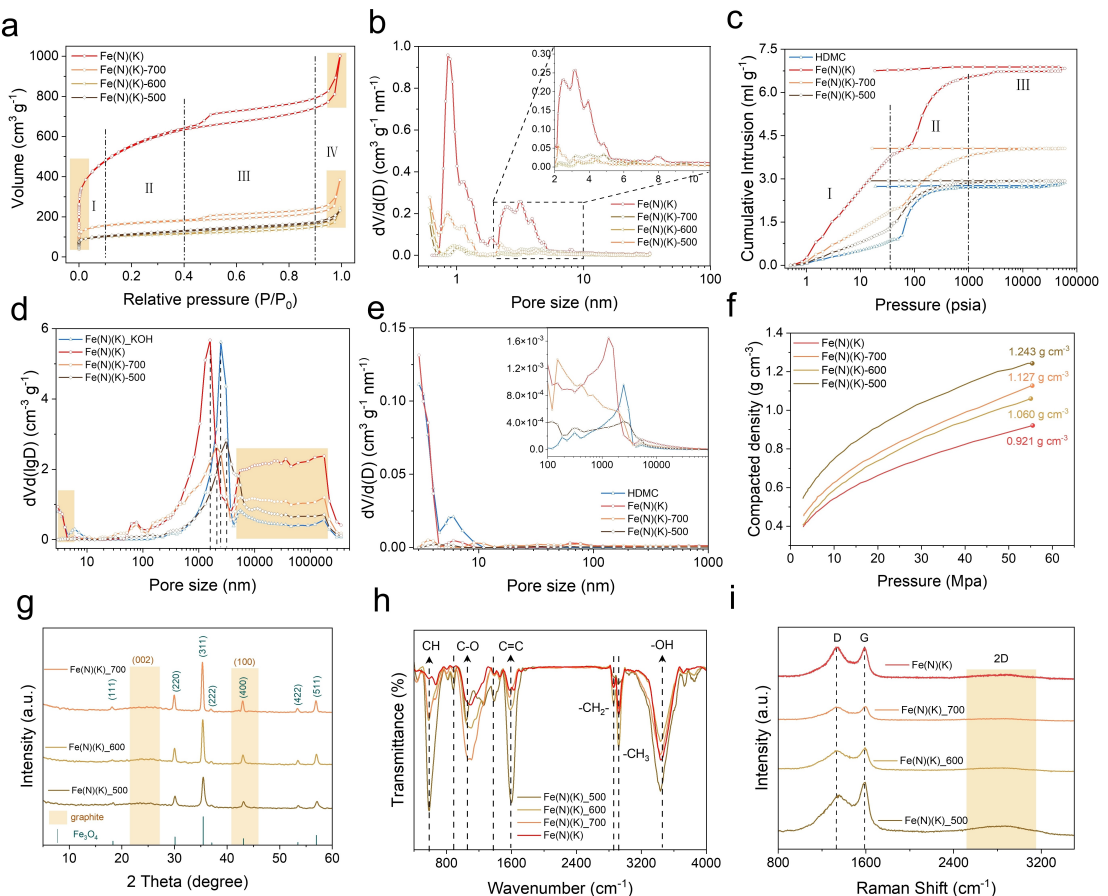


Figure 4. a) Isothermal adsorption/desorption curves of Fe(N)(K)_500, Fe(N)(K)_600, Fe(N)(K)_700 and Fe(N)(K). b) Pore size distribution analyzed from isothermal curves by DFT method. c) Mercury intrusion curve (0–80000 psia) of HDMC, Fe(N)(K), Fe(N)(K)_500 and Fe(N)(K)_700. d) The distribution of pore volume analyzed from MIP curves. e) The differential pore volume distribution analyzed from MIP curves. f) Characterization of compacted density at different pressure for Fe(N)(K)_500, Fe(N)(K)_600, Fe(N)(K)_700 and Fe(N)(K). g) XRD curves (5–60°) of Fe(N)(K)_500, Fe(N)(K)_600 and Fe(N)(K)_700. h) FTIR curves (400–4000 cm⁻¹) of Fe(N)(K)_500, Fe(N)(K)_600, Fe(N)(K)_700 and Fe(N)(K). i) Raman curves (800–3600 cm⁻¹) of Fe(N)(K)_500, Fe(N)(K)_600, Fe(N)(K)_700 and Fe(N)(K).

could be retained after second-activation. Tortuosity refers to the ratio of pore channels path to average carbon particles size, benefiting from the controllable pores-etching ability of multiple dimensional activation strategy. HDMC presents the lowest tortuosity of 2.4055. Its pore structure could provide wide space size distribution and excellent connectivity simultaneously, which is beneficial for HDMC-based electrodes to maintain the balance of ion concentration in the pore channel at high power density. Compare with Fe(N)(K) (6.8339 mg⁻¹ and 0.1210 g cm⁻³), the lower total intrusion volume and higher bulk density of HDMC (2.8652 mg⁻¹ and 0.2371 g cm⁻³) evidently suggested that second-activation effectively should reduce the roughness of carbon surface and optimize the configuration of carbon skeleton. Figure 4f further reveals the changes of compacted density during first-activation. Compacted density decreases with the increase of the activation temperature, which proves that the pore-forming etching reaction is carried out during all first-activation stage. Fe(N)(K) carbon skeleton demonstrate the etching ratio of 25.9% (500–800 °C). During the activation reaction process, a significant amount of Fe(N)(K) on the carbon pore wall primarily occurs at temperatures ranging from 600 to 800 degrees Celsius. The

etching reaction intensifies with increasing temperature; conversely, at 500 degrees Celsius, minimal etching occurs, resulting in a higher compaction density.

In Figure 4g, XRD curves further reveal the transformation mechanism of FeO_x activator during first-activation. Obvious Fe₃O₄ sharp peaks (PDF#97-015-9963) in Fe(N)(K)_500, Fe(N)(K)_600 and Fe(N)(K)_700 proved all the FeO_x components in different first-activated carbon are eventually transformed into Fe₃O₄. Also, the changing surface functional groups from first-activated carbon were characterized by FTIR curves (Figure 4h). As the temperature increases, the relative intensity ratio of CH, C=O groups to C=C bonds reduces, which could be attributed to the decomposition of cellulose and the increasing proportion of stable-C element. Intensity of -OH group first decreased (500–600 °C) then increased (600–800 °C), which could be ascribed to the introduction of polar surface groups by KCl molecule at higher reaction temperature. Furthermore, disorder degree of carbon skeleton were analyzed by Raman spectroscopy (Figure 4i). The D peak get narrowed with the increase of temperature, I_d/I_g ratio reaches maximum of 2.40 at 700 °C (Figure S9), suggestive of the formation of disordered carbon structures (irregular macropore and rough surfaces) during

500–700 °C etching temperatures by FeO_x . While KCl component is beneficial to improve the uniformity of hierarchical pores and stable skeleton during 700–800 °C. Compared to $\text{Fe}(\text{N})(\text{K})_{500}$ and $\text{Fe}(\text{N})(\text{K})$, the weaker 2D peaks of $\text{Fe}(\text{N})(\text{K})_{600}$ and $\text{Fe}(\text{N})(\text{K})_{700}$ also reveal that FeO_x should play a major role on cellulose to form a disordered graphite structure.

To reveal and differentiate the synergistic pore-forming mechanism between Fe_2O_3 and KCl activator, isothermal adsorption/desorption method were employed to characterize the activated samples by $\text{Fe}(\text{NO}_3)_3$ ($\text{Fe}(\text{N})$), KCl ($\text{Fe}(\text{K})$), and without activator (AC-800). As shown in Figure 5a and Table S7, AC-800 and $\text{Fe}(\text{K})$ with type-I adsorption characteristic demonstrate the lower SSA of $590.5 \text{ m}^2 \text{ g}^{-1}$ and $770.0 \text{ m}^2 \text{ g}^{-1}$. Compared with $\text{Fe}(\text{N})(\text{K})$, $\text{Fe}(\text{N})$ with type-IV characteristic suggests the smaller adsorption volume and the more obvious hysteresis loop characteristic, indicative of the larger mesoporous by FeO_x etching. Also, the larger average pore size of $\text{Fe}(\text{N})$ (3.544 nm) than that of $\text{Fe}(\text{K})$ (2.199 nm) suggests the forming mesopores should be dominated by FeO_x and further the smaller pores should be constructed by KCl molecules. In Figure 5b, the mesopore sizes of $\text{Fe}(\text{N})(\text{K})$ is between 2–5 nm, while that of $\text{Fe}(\text{N})$ is between 5–32 nm. This pore distribution proves the above pore-forming mechanism. For the mesopore volume (Figure 5c), $\text{Fe}(\text{N})(\text{K})$ ($\beta_{\text{Fe}(\text{N})(\text{K})} = 23.4\%$) present the higher mesoporous ratio than $\text{Fe}(\text{K})$ and AC-800 ($\beta_{\text{Fe}(\text{K})} = 18.8\%$, $\beta_{\text{AC-800}} = 23.2\%$), suggesting the more efficient mesopores construction ability of $\text{Fe}(\text{NO}_3)_3$ activator. While $\text{Fe}(\text{N})(\text{K})$ present the lower mesoporous ratio than $\text{Fe}(\text{N})$ ($\beta_{\text{Fe}(\text{N})} = 50.4\%$), suggesting the smaller micropores construction ability of KCl molecule for the balance of mesoporous proportion. The excessive mesoporous of $\text{Fe}(\text{N})(\text{N})$ restricts the utilization of its pore volume and results in low density carbon skeleton. In detail, the $\text{Fe}(\text{NO}_3)_3$ activator constructs the hierarchical pore channels during the low-

temperature of 500–700 °C. Based on these channels, the rapidly-diffused KCl activator will reduce the reaction barrier during the high-temperature of 700–800 °C toward the more efficient construction of micropore. So, $\text{Fe}(\text{N})(\text{K})$ can obtain an ideal proportion of micropore/mesoporous. This multi-dimensional activation mechanism finally constructs a hierarchical skeleton-pore system with rich active sites and interconnected channels.

To explore the universality of the multi-dimensional activation mechanism and reveal the different activation ability of ferric salts. The isothermal adsorption/desorption method was applied to insight into the activated samples by $\text{Fe}_2(\text{SO}_4)_3$ ($\text{Fe}(\text{S})$), $\text{Fe}_2(\text{SO}_4)_3@\text{KCl}$ ($\text{Fe}(\text{S})(\text{K})$), FeCl_3 ($\text{Fe}(\text{Cl})$), and $\text{FeCl}@KCl$ ($\text{Fe}(\text{Cl})(\text{K})$). As shown in Figures 5d,e and Table S8, $\text{Fe}(\text{S})$ and $\text{Fe}(\text{Cl})$ present the more obvious hysteresis loop characteristic and the larger number mesopores than $\text{Fe}(\text{S})(\text{K})$ and $\text{Fe}(\text{Cl})(\text{K})$, indicating mesopores were mostly formed during low-temperature process. But $\text{Fe}(\text{S})(\text{K})$ and $\text{Fe}(\text{Cl})(\text{K})$ show the larger SSA ($1178 \text{ m}^2 \text{ g}^{-1}$ @ $1023 \text{ m}^2 \text{ g}^{-1}$) and smaller average pore size (2.975 nm @ 3.088 nm) than $\text{Fe}(\text{S})$ and $\text{Fe}(\text{Cl})$ ($727.5 \text{ m}^2 \text{ g}^{-1}$ @ $899.6 \text{ m}^2 \text{ g}^{-1}$ and 3.650 nm @ 3.285 nm). For the mesopore proportion (Figure 5f), $\text{Fe}(\text{S})$ ($\beta_{\text{Fe}(\text{S})} = 38.4\%$), $\text{Fe}(\text{Cl})$ ($\beta_{\text{Fe}(\text{Cl})} = 41.9\%$) and $\text{Fe}(\text{N})$ ($\beta_{\text{Fe}(\text{N})} = 50.4\%$) demonstrate the larger proportion of mesopores than $\text{Fe}(\text{S})(\text{K})$ ($\beta_{\text{Fe}(\text{S})(\text{K})} = 27.3\%$), $\text{Fe}(\text{Cl})(\text{K})$ ($\beta_{\text{Fe}(\text{Cl})(\text{K})} = 27.3\%$) and $\text{Fe}(\text{N})(\text{K})$ ($\beta_{\text{Fe}(\text{N})(\text{K})} = 23.4\%$), proving that the multi-component activator could construct a more reasonable proportion of mesopores than the single-component activator.

To reveal energy storage properties of HDMC. For three-electrode supercapacitor with aqueous-type, HDMC reveal higher specific capacitance of 302.3 F g^{-1} than the commercial carbon YP-50F (143.3 F g^{-1}) (Figure 6a), capacitances retention ratio (1–80 A g^{-1}) of HDMC and YP-50F are 80.6% and 84.0%,

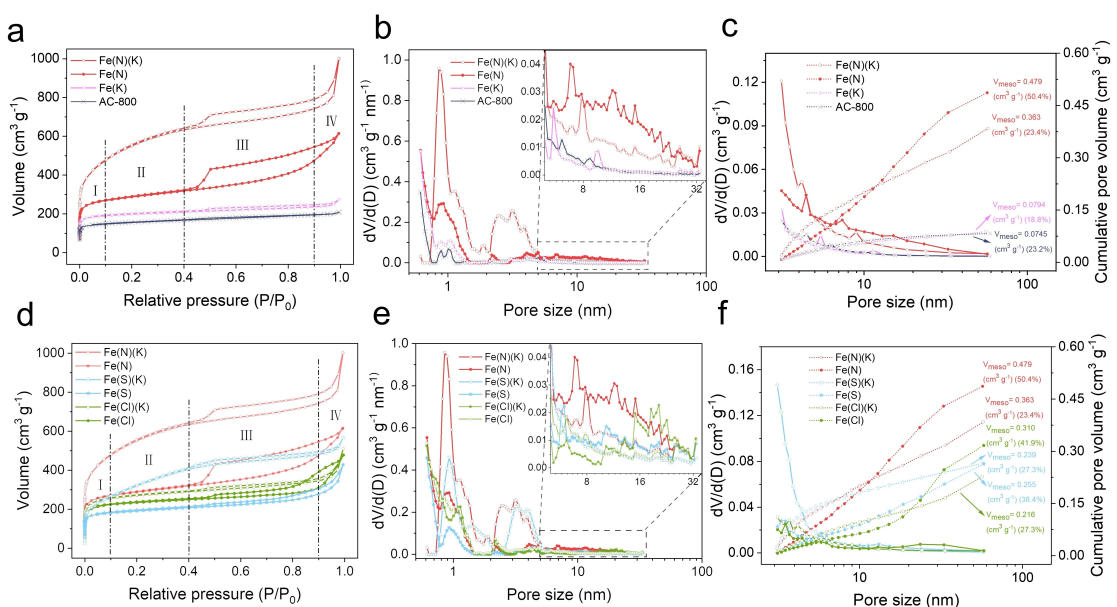


Figure 5. a) Isothermal adsorption/desorption curves of $\text{Fe}(\text{N})$, $\text{Fe}(\text{K})$, AC-800, $\text{Fe}(\text{N})(\text{K})$ and b) their pore size distribution analyzed from isothermal curves by DFT method, c) their cumulative volume and pore size analyzed from isothermal curves by BJH method. d) Isothermal adsorption/desorption curves of $\text{Fe}(\text{N})(\text{S})$, $\text{Fe}(\text{S})$, $\text{Fe}(\text{Cl})(\text{K})$, $\text{Fe}(\text{Cl})$, $\text{Fe}(\text{N})(\text{K})$, $\text{Fe}(\text{N})$ and e) their pore size distribution analyzed from isothermal curves by DFT method, f) their cumulative volume and pore size analyzed from isothermal curves by BJH method.

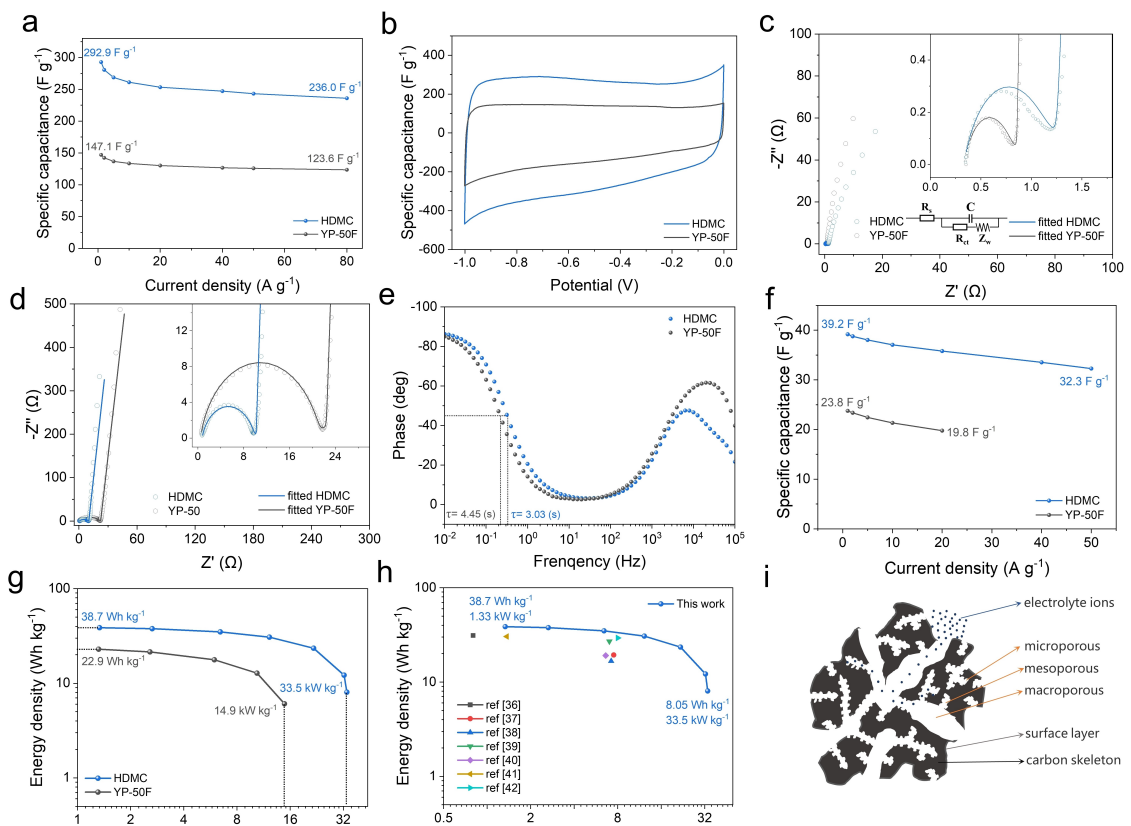


Figure 6. Electrochemical property of HDMC and YP-50F analyzed by three-electrode devices (aqueous electrolyte) and symmetric supercapacitor (organic electrolyte). a) Rate performance (current density from 1–80 A g⁻¹). b) CV curves (scan rate for 10 mV s⁻¹). c) and d) Nyquist plot (characterized at 0.01–100000 Hz, 10 mV s⁻¹). e) Bode plot. f) Rate performance (current density from 1–50 A g⁻¹) g) Relation between energy density and power density. h) Power/energy density performance compared with other reported work.^[34–40] i) Theoretical ion-electron transport model of HDMC.

HDMC electrode not only demonstrate high capacitance at low power, but also show excellent electrochemical performance for higher power. In Figure 6b, there are no obvious redox peaks shown in CV curves (10 mV s⁻¹), demonstrates ideal energy storage mechanism of electric double layer capacitor of HDMC. For impedance characteristic, HDMC present the lower ohmic resistance ($R_s=0.3337\ \Omega$) and the higher transfer resistance ($R_{ct}=0.8369\ \Omega$) than the commercial YP-50F (0.3411 Ω and 0.4698 Ω), respectively, higher R_{ct} could attributed to the incompatibility that aqueous-type electrolyte is difficult to infiltrate into HDMC higher purity C element skeleton (Figure 6c). While for symmetrical supercapacitor with ET_4NBF_4 electrolyte, HDMC present lower ohmic resistance and transfer resistance (0.3337 Ω and 9.079 Ω) than YP-50F (0.4664 Ω and 20.61 Ω) (Figure 6d). And as shown in Figure 6e, HDMC also demonstrate lower electrochemical relaxation time (τ) than YP-50F (3.03 s@4.45 s). Different from aqueous electrolyte, the excellent response characteristic of HDMC is not only attribute to its larger proportion of mesopores that are compatible to larger-sized ions, but also related to ideal wettability to organic-type electrolytes. Therefore, HDMC-based supercapacitor could be adapted for higher working power, which device provide high specific capacitance of 39.2 F g⁻¹ at 1 A g⁻¹ current density and 82.4% capacitance-remaining at 50 A g⁻¹ Figure 6f. Meanwhile, the super-high power density of 33.5 kW kg⁻¹ with an

energy density of 8.05 Wh kg⁻¹ for HDMC is not only better than YP-50F (14.9 kW kg⁻¹@0.06 Wh kg⁻¹) (Figure 6g), its high power performance is also excelled than most of the reported carbon materials (Figure 6i). The electrochemical process model of HDMC electrode is shown in Figure 7j, ions could rapidly move through the hierarchically mesoporous channel, and the electrons could efficiently transfer along the densifying carbon skeleton.

To further proved the feasibility of hierarchically-densifying construct strategy and compare the advantages of high-density electrode materials in volume performance, producing steps of HDMC was amplified, and as developed HDMC-based supercapacitor could support miniature lamps working continuously for more than 300 s, indicate the excellent application potential of HDMC (Figure 7a). Higher density property of porous carbon electrode is beneficial to improve the specific volume performance of supercapacitor. The relation between thickness and the loading mass of electrode sheet was shown in Figure 7b. HDMC show larger average loading density of 0.363 g cm⁻³ than that of Fe(N)(K) (0.301 g cm⁻³) and close to YP-50F (0.356 g cm⁻³), which strong proved that the density for HDMC electrode effectively increase by the strategy of densification treatment. It is incriminated to HDMC provide more excellent dispersion performance for its-based slurry, the invalid particle gap space is lesser, thereby improving the volume performance of the

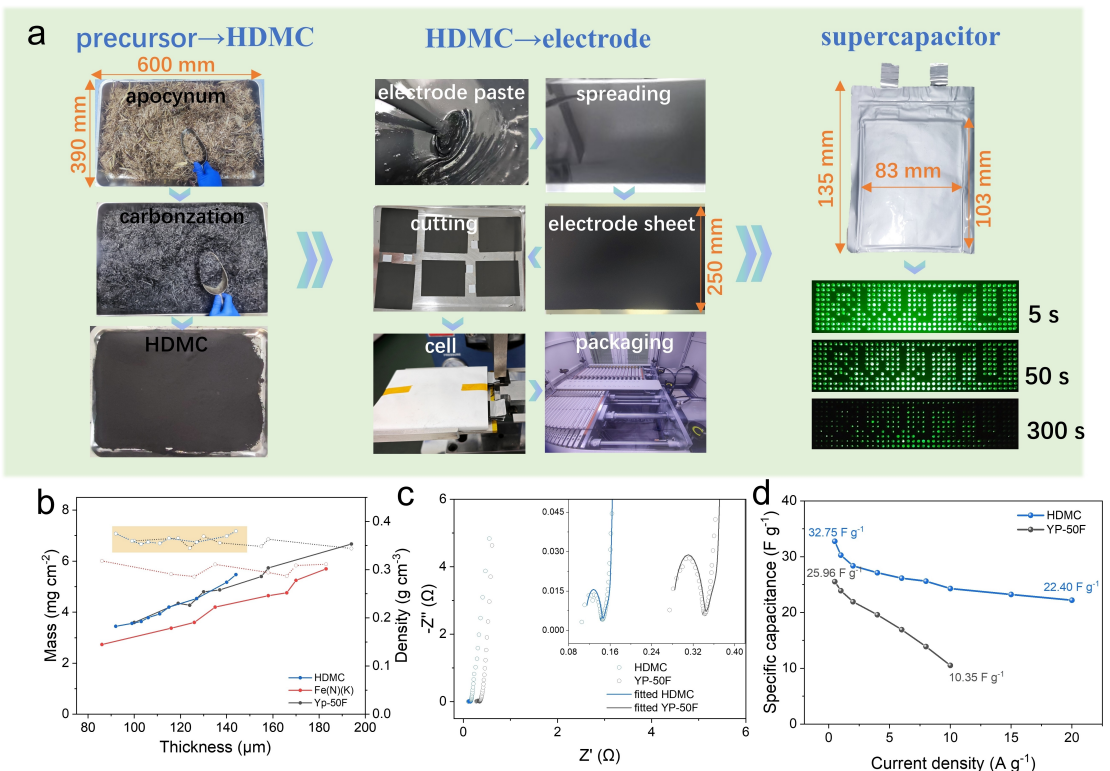


Figure 7. a) The feasibility proof of hierarchically-densifying construction strategy. b) Relation between thickness of spreading layer and loading mass of electrode. c) Nyquist plot (characterized at 0.01–100000 Hz, 10 mVs⁻¹) of HDMC and YP-50F. d) Rate performance (current density from 1–20 Ag⁻¹) of HDMC and YP-50F.

spreading layer. Comparing the Nyquist plot (Figure 7c), HDMC-based supercapacitor reveal lower ohmic resistance ($R_s=0.112\ \Omega$) and transfer resistance ($R_{ct}=0.0318\ \Omega$) than YP-50 F ($R_s=0.279\ \Omega$, $R_{ct}=0.0618\ \Omega$), which again prove that with high density and hierarchically pore structure of HDMC electrode for the advantage of fast electrochemical response compared with the commercial carbon of material YP-50F. The rate performance were also shown in Figure 7d, HDMC could provide high capacitance of 32.75 F g^{-1} at 1 Ag^{-1} current density or 22.40 F g^{-1} capacitance at 20 Ag^{-1} , and for the specific volume performance, HDMC could provide the higher specific volume energy density of 11.0 Wh L^{-1} (1 Ag^{-1}) or the high specific volume power density of 9.37 kW L^{-1} (20 Ag^{-1}), which is superior to YP-50F (7.49 Wh L^{-1} at 1 Ag^{-1} or 4.63 kW L^{-1} at 10 Ag^{-1}). It is obvious proved that the densifying HDMC could provide advantages in improving the volume performance of supercapacitor.

For electrochemical characterization, on the one hand, through the multi-dimensional activation strategy which construct an ideal proportion of micro-mesoporous structure, the established interconnect and wide-size pore channels shorten the ion transport path and provide excellent ionic conductivity for the electrochemical process. On the other hand, the densification treatment constructs a skeleton structure with high continuity and high electronic conductivity. Basis on rich active sites and stable pore-skeleton system, HDMC could reveal

more excellent high-power and high specific volume performance than the traditional microporous-type carbon electrode.

Such superior rate performance and specific volume performance of HDMC-based power type supercapacitor is ascribed to the multi-dimensional first-activation strategy for constructing higher proportion of mesoporous and the second-activation strategy for constructing densifying carbon skeleton. Firstly, by using composite activator of $\text{Fe}(\text{NO}_3)_3\text{-KCl}$, the construction processes of micropores and mesopores are divided into different activation steps. This multi-dimensional activation strategy greatly improves the mesoporous proportion of HDMC, which is beneficial for ions transport faster and working at higher power. Secondly, the secondary activation strategy reduces the surface roughness of HDMC, which forms a stacking morphology of carbon particles with higher space utilization and construct a continuous carbon skeleton system. Therefore, the excellent high-power performance and specific volume performance of HDMC is proved to the synergistic effect of pore structure with high ionic conductivity and densifying skeleton structure with high electronic conductivity. Both electrons and ions transport faster through the dense skeleton and hierarchical pore system of HDMC, thereby its-based supercapacitor could exhibit better storage performance for higher power.

For HDMC, potential low-cost strategies include using abundant precursor materials, such as agricultural waste or industrial by-products, which are relatively low in cost. In

addition, adopting simple and scalable preparation processes, such as direct activation or template methods, can reduce production costs. As for large-scale production, preliminary plans may include establishing automated and continuous production lines to improve production efficiency and output. Moreover, the rational layout and optimization of production facilities, as well as improvements in supply chain management, are also key factors in achieving large-scale production. During the production process, strict quality control and the establishment of standardized processes help ensure the consistency and reliability of product quality.

3. Conclusions

In conclusion, we build hierarchical densified mesoporous biomass-based carbon by the strategy of multi-dimensional activation and strategy of densified carbon surface modification. Benefit from the excellent physical properties of high SSA ($2130 \text{ m}^2 \text{ g}^{-1}$), high tap density (0.387 g cm^{-3}), ideal micro-porous-mesoporous system (23.1 % proportion of mesoporous) and high conductivity ($2.6 \times 10^3 \text{ S m}^{-1}$) continuous carbon skeleton structure. HDMC electrode could provide high theoretical capacitance of 292.9 F g^{-1} (aqueous-type electrolyte). HDMC-based supercapacitor reveal superior rate performance, which could provide high power density of 33.5 kW kg^{-1} at energy density of 8.05 Wh kg^{-1} and demonstrate 82.4% capacitance-remaining (1–50 A g $^{-1}$). Meanwhile, as-papered soft packaging supercapacitor devices also demonstrate ideal high volume performance of HDMC, which reveal high electrode density of 0.363 g cm^{-3} , superior in specific volume power density of 9.37 kW L^{-1} and specific volume energy density of 11.0 Wh L^{-1} . These results strongly demonstrate that the multi-dimensional activation and densification strategy could effectively construct porous carbon which is suitable for power-type supercapacitor electrode. The properties of low cost and large-scale preparation for this HDMC also reveals its prospect for applying in electrochemical energy storage.

Experimental

Materials

Natural apocynum was obtained from Xinjiang, China. Iron nitrate ($\text{Fe}(\text{NO}_3)_3$), iron sulfate ($\text{Fe}_2(\text{SO}_4)_3$), ferric chloride ($\text{Fe}(\text{Cl})_3$), carboxymethyl cellulose (CMC), polytetrafluoroethylene (PTFE) were purchased from Shanghai Aladdin Co. Potassium hydroxide (KOH), hydrochloric acid (HCl) and isopropanol (IPA) were purchased from Chengdu Kelon Chemical Co. As contrast commercial capacitive carbon (YP-50F) was purchased from Kuray Co. Conductive carbon (Super C45) was purchased from Tianjin Annuhe Technology Co. Tetraethylammonium tetrafluoroborate (Et_4NBF_4) electrolyte (DLC-301) were purchased from Shenzhen Capchem Co. Button battery shell, nickel foam, aluminum foil, cellulose separator used in device packaging were purchased from Tianjin Damao chemical reagent Co.

Preparation of Precursor

Firstly, break the natural apocynum. Secondly, three impregnation solutions samples ($\text{Fe}(\text{N})(\text{K})$, $\text{Fe}(\text{S})(\text{K})$, $\text{Fe}(\text{Cl})(\text{K})$) were prepared respectively (apocynum : molysite : KCl : deionized water = 1:0.5:1:6). For $\text{Fe}(\text{N})(\text{K})$ impregnation solution, 5 g crushed apocynum, 2.5 g $\text{Fe}(\text{NO}_3)_3$ and 5 g KCl are add in 30 ml of deionized water and evenly mix. For $\text{Fe}(\text{S})(\text{K})$ and $\text{Fe}(\text{Cl})(\text{K})$ impregnation solutions, $\text{Fe}(\text{NO}_3)_3$ is replaced by $\text{Fe}_2(\text{SO}_4)_3$ and FeCl_3 . Thirdly, impregnation solutions were heated to 70°C for 12 h in air blast drying oven (101-2B, Yuanyan Instrument Co.), after cooling to 25°C , filter the remaining solution. Finally, continue drying the samples for 12 h at 90°C , and three precursors to be carbonized are obtained. And for control precursor samples ($\text{Fe}(\text{N})$, $\text{Fe}(\text{S})$, $\text{Fe}(\text{Cl})$) (apocynum : molysite : deionized water = 1:0.5:6) were also prepared with the same process.

Preparation of First-Activation Samples

For each precursor, 2 g precursor was carbonized and activated at 800°C for 2 h in a tube furnace (BTF-1200 C, Anhui Beyick Equipment Co.) (heating rate is 3°C min^{-1} and protected with 80 ml min^{-1} argon). After cool to 25°C , the obtained samples were reacted with HCl solution and adjust the PH of the system to 1. After stirring for 6 h, use deionized water to repeatedly filter and clean until PH = 7, then drying samples for 12 h at 100°C . Finally, the obtained carbon was ground to complete first-activation process. For control samples of $\text{Fe}(\text{N})(\text{K})$ -700, $\text{Fe}(\text{N})(\text{K})$ -600 and $\text{Fe}(\text{N})(\text{K})$ -500, $\text{Fe}(\text{N})(\text{K})$ precursor was activated at 700°C , 600°C and 500°C , respectively. For control samples of $\text{Fe}(\text{N})$ and $\text{Fe}(\text{K})$, precursor was activated by single activator component of $\text{Fe}(\text{NO}_3)_3$ or KCl at 800°C .

Preparation of Second-Activation Samples

The first activated $\text{Fe}(\text{N})(\text{K})$ was mixed with KOH ($\text{Fe}(\text{N})(\text{K})$: KOH = 1:2), then heating the mixture (1 g) to 800°C for 2 h in tube furnace (heating rate is 3°C min^{-1} and protected with 80 ml min^{-1} argon). After the same parameters of cooling, reaction with hydrochloric acid solution, cleaning and drying steps. HDMC (which also named $\text{Fe}(\text{N})(\text{K})$ -KOH) was obtained. For control sample of AC-KOH, apocynum was mixed with KOH (apocynum : KOH = 1:2) to form the mixture, activation and subsequent treatment were performed by the same steps. For control sample of Ap-800, 1 g apocynum was directly activated without activator. For proving the product feasibility of HDMC, the carbonization and activation process of precursor were carried out in a rotary resistance furnace (Xianyan Honfeng Co, HF-RZ20.60).

Characterization

Surface morphology of HDMC was characterized by scanning electron microscopy (SEM, EM-30AX+). The shape, distribution of micropores and mesopores were observed by transmission electron microscopy (TEM, JEM-2100F). The surface composition and distribution of different elements are observed by energy dispersive spectroscopy (SEM-EDS mapping) (OXFROD X-Max 80). Fourier transform infrared spectroscopy analyzer (FTIR, Bruker TENSOR II) was used to analyze the composition of surface functional group. X-ray diffractometer (Cu-K α source (0.154 nm)) (XRD, DX-2700BH) was used to analyzed the crystal structure of porous carbon and chemical changes of activators. Raman spectrometer (532 nm laser) (Lab RAM HREvolution) was used to analyze the structure of graphite and the disorder degree of its stacking type. X-ray photoelectron spectroscopy (XPS, Thermo ESCALAB 250Xi) was used to characterize the composition and proportion of chemical

bond. The change between conductivity and density is characterized by a compaction density analyzer (ROOKO FT-8600). The loose density and tap density were analyzed by a powder cone density analyzer (FT-100E-3). The specific surface area (SSA), pore size distribution and other related pore parameters were analyzed by a automated gas sorption analyzer (Anton Paar Autosorb IQ) (N_2) is used as adsorbent, all samples were dried in vacuum at 250 °C for 3 h. it may not accurately measure larger pores. Mercury porosimeter (MP, Micromeritics AutoPore IV 9500) was used to analyzed mesoporous, macroporous, interstitial space and tortuosity. It is suitable for analyzing pores from micrometers to nanometers in size.

Electrochemical Measurements

For the three-electrode supercapacitor devices, use KOH solution (6 mol L⁻¹) as electrolyte, and electrode paste is composed of the prepared capacitive active material, conductive material (Super C45) and agglomerant (10% PTFT) with mass ratio of 8:1:1 in IPA solution. The paste is dried at 80 °C for 5 h to remove excess IPA, then evenly coat paste on the nickel foam and roll. After drying in 100 °C for 12 h, the working electrode was obtained. The electrochemical characteristic (Galvanostatic charge/discharge (GCD), cyclic voltammetry (CV) and electrochemical impedance spectroscopy (EIS)) of working electrode were characterized by electrochemical workstation (uidstat Prime and Squidstat Plas).

For the symmetric supercapacitor, electrode paste is composed of active material, Super C45 and 1% CMC with mass ratio of 85:10:5. The past was coated on the aluminum foil, after drying (100 °C for 12 h) and rolling, cut aluminum foil to obtain electrode sheets as positive and negative. Then, electrode sheets were assembled in the button battery or soft packaging supercapacitor with Et₄NBF₄ electrolyte. Besides the electrochemical characterization of GCD, CV and EIS, cycle life of supercapacitor was also analyzed by Arbin MSTAT4 (Arbin Instruments Co).

Specific capacitance (C, F g⁻¹) of supercapacitor was calculated from discharge process of GCD method, as follow:

$$C = \frac{I\Delta t}{m\Delta V}$$

Where I (A) is the current, Δt is the discharge time, m (g) is the mass of capacitive active material in electrode. ΔV (V) is the working voltage range.

$$E = \frac{1}{2} C(\Delta V)^2$$

Energy density (E, Wh kg⁻¹) and power density (P, kW kg⁻¹) could be calculated from specific capacitance, as following formula:

$$P = \frac{E}{\Delta t}$$

Where C (F g⁻¹) is as calculated specific capacitance, ΔV (V) is the working voltage range, Δt is the working time of discharge step.

Acknowledgements

This work was supported by the National Natural Science Foundation of China (No. 52372228).

Conflict of Interests

The authors declare no competing financial interest.

Data Availability Statement

The data that support the findings of this study are available from the corresponding author upon reasonable request.

Keywords: Porous carbon • Supercapacitor • Super-high power • Densifying • Biomass

- [1] M. Z. Zhong, M. Zhang, X. F. Li, *Carbon Energy* **2022**, *4* (5), 950–985.
- [2] D. P. Chatterjee, A. K. Nandi, *J. Mater. Chem. A* **2021**, *9*, 15880–15918.
- [3] W. J. Dong, M. Xie, S. W. Zhao, Q. L. Qin, F. Q. Huang, *Mater. Sci. Eng. R-Rep.* **2023**, *152*, 100713.
- [4] X. S. Hu, D. X. Zuo, S. R. Cheng, S. H. Chen, Y. Liu, W. Z. Bao, S. L. Deng, S. J. Harris, J. Y. Wan, *Chem. Soc. Rev.* **2023**, *52*, 1103–1128.
- [5] Y. X. Wang, T. Xu, K. Liu, M. Zhang, X. M. Cai, C. L. Si, *Aggregate* **2024**, *5*, e428.
- [6] Y. F. Yin, Q. J. Liu, Y. T. Zhao, T. T. Chen, J. Wang, L. Gui, C. Y. Lu, *Energy Fuels* **2023**, *37*, 3523–3554.
- [7] Y. Yang, D. M. Chen, W. B. Han, Y. Cheng, B. Q. Sun, C. L. Hou, G. D. Zhao, D. Z. Liu, G. Q. Chen, J. C. Han, X. H. Zhang, *Carbon* **2023**, *205*, 1–9.
- [8] Z. X. Xu, W. J. Deng, X. L. Wang, *Electrochim. Energy Rev.* **2021**, *4*, 269–335.
- [9] S. L. Wu, Y. W. Zhu, *Sci. China Mater.* **2017**, *60*, 25–38.
- [10] S. Sundriyal, V. Shrivastav, H. D. Pham, S. Mishra, A. Deep, D. P. Dubal, *Resour. Conserv. Recycl.* **2021**, *169*, 105548.
- [11] X. H. Zhang, R. Y. Han, Y. Z. Liu, H. X. Li, W. J. Shi, X. Y. Yan, X. X. Zhao, Y. F. Li, B. S. Liu, *Chem. Eng. J.* **2023**, *460*, 141607.
- [12] J. Q. Zhou, S. L. Zhang, Y. N. Zhou, W. Tang, J. H. Yang, C. X. Peng, Z. P. Guo, *Electrochim. Energy Rev.* **2021**, *4*, 219–248.
- [13] R. Yuksel, N. Karakehya, *Carbon* **2024**, *221*, 118934.
- [14] G. Jeanmairet, B. Rotenberg, M. Salanne, *Chem. Rev.* **2022**, *122*, 10860–10898.
- [15] P. Li, T. X. Shang, X. M. Dong, H. Li, Y. Tao, Q. H. Yang, *Small* **2021**, *17*, 2007548.
- [16] Y. A. Kumar, G. Koyyada, T. Ramachandran, J. H. Kim, S. Sajid, M. Moniruzzaman, S. Alzahmi, I. M. Obaidat, *Nanomaterials* **2023**, *13*, 1409.
- [17] Z. H. Bi, Q. Q. Kong, Y. F. Cao, G. H. Sun, F. Y. Su, X. X. Wei, X. M. Li, A. Ahmad, L. J. Xie, C. M. Chen, *J. Mater. Chem. A* **2019**, *7*, 16028–16045.
- [18] W. Y. Long, B. Z. Fang, A. Ignaszak, Z. Z. Wu, Y. J. Wang, D. Wilkinson, *Chem. Soc. Rev.* **2017**, *46*, 7176–7190.
- [19] S. K. Das, L. Pradhan, B. K. Jena, S. Basu, *Carbon* **2023**, *201*, 49–59.
- [20] H. L. Qin, P. Liu, C. R. Chen, H. P. Cong, S. H. Yu, *Nat. Commun.* **2021**, *12*, 4297.
- [21] Q. Wang, Z. Y. Chen, Q. T. Luo, H. J. Li, J. Li, W. Q. Yang, *Small* **2023**, *19*, 2303349.
- [22] Y. D. Zhang, R. Shao, W. Xu, J. F. Ding, Y. Wang, X. H. Yan, W. Y. Shi, M. Wang, *Chem. Eng. J.* **2021**, *419*, 129576.
- [23] H. L. Li, Y. L. Liu, H. T. Jin, L. H. Cao, H. Q. Yang, S. H. Jiang, S. J. He, S. S. Li, K. M. Liu, G. G. Duan, *Diamond Relat. Mater.* **2022**, *128*, 109283.
- [24] T. Zhao, Y. Yao, Y. F. Yuan, M. L. Wang, F. Wu, K. Amine, J. Lu, *Nano Energy* **2021**, *82*, 105782.
- [25] B. Yan, J. J. Zheng, L. Feng, Q. Zhang, C. M. Zhang, Y. C. Ding, J. Q. Han, S. H. Jiang, S. J. He, *Mater. Des.* **2023**, *229*, 111904.
- [26] L. Luo, Y. L. Lan, Q. Q. Zhang, J. P. Deng, L. C. Luo, Q. Z. Zeng, H. L. Gao, W. G. Zhao, *J. Storage Mater.* **2022**, *55*, 105839.
- [27] Y. Sun, X. L. Shi, Y. L. Yang, G. Q. Suo, L. Zhang, S. Y. Lu, Z. G. Chen, *Adv. Funct. Mater.* **2022**, *32*, 2201584.
- [28] B. Singh, M. B. Gawande, A. D. Kute, R. S. Varma, P. Fornasiero, P. McNeice, R. V. Jagadeesh, M. Beller, R. Zboril, *Chem. Rev.* **2021**, *121*, 13620–13697.
- [29] S. W. Xia, H. P. Yang, S. S. Lei, W. Lu, N. Cai, H. Y. Xiao, Y. Q. Chen, H. P. Chen, *Energy* **2023**, *262*, 125415.
- [30] L. Frankenstein, P. Glomb, J. Ramirez-Rico, M. Winter, T. Placke, A. Gomez-Martin, *ChemElectroChem* **2023**, *10*, e202201073.

- [31] J. Y. Liu, X. Zhang, H. Peng, T. Q. Li, P. Liu, H. R. Gao, Y. T. Wang, J. F. Tang, Q. Li, Z. Qi, L. C. Peng, T. Xia, *Molecules* **2023**, *28*, 2060.
- [32] B. R. Zhang, F. Sun, Y. Li, D. Y. Wu, C. L. Yang, Z. F. Wang, J. H. Gao, G. B. Zhao, S. Z. Sun, *Carbon* **2024**, *219*, 118812.
- [33] T. T. Zhu, Z. Y. Song, J. M. Lin, L. Q. Fan, J. Y. Lin, J. H. Wu, *Electrochim. Acta* **2022**, *405*, 139827.
- [34] H. Zheng, Q. P. Cao, M. N. Zhu, D. Xu, H. Y. Guo, Y. Li, J. H. Zhou, *J. Mater. Chem. A* **2021**, *9*, 10120–10134.
- [35] H. A. Hamouda, H. I. Abdu, Q. Z. Hu, M. A. Abubaker, H. K. Lei, S. Z. Cui, A. I. Alduma, H. Peng, G. F. Ma, Z. Q. Lei, *Front. Chem.* **2022**, *10*, 1024047.
- [36] X. Zhao, M. Sajjad, Y. Q. Zheng, M. M. Zhao, Z. J. Li, Z. Y. Wu, K. Kang, L. Qiu, *Carbon* **2021**, *182*, 144–154.
- [37] Y. H. Bao, H. Xu, Y. Q. Zhu, P. D. Chen, Y. J. Zhang, Y. Chen, *Electrochim. Acta* **2023**, *437*, 141533.
- [38] J. Vazquez-Samperio, G. Ramírez-Campos, M. A. León-Luna, F. Echevarría, A. Cano, A. Hernández-Gordillo, P. Acevedo-Peña, E. Reguera, *Electrochim. Acta* **2021**, *380*, 138218.
- [39] P. G. Qi, J. X. Wang, L. R. Yang, Y. H. Su, W. Zhu, M. Jiang, X. F. Sun, P. Zhang, Y. Q. Xiong, *J. Alloys Compd.* **2023**, *960*, 170804.
- [40] C. Q. Zheng, H. Gong, Y. W. Jiang, B. Chen, Y. Y. Su, J. H. Zhou, Y. Li, *ACS Appl. Nano Mater.* **2023**, *6*, 14136–14150.

Manuscript received: July 2, 2024

Revised manuscript received: September 19, 2024

Accepted manuscript online: October 10, 2024

Version of record online: November 13, 2024